Ocean Engineering 286 (2023) 115612

Contents lists available at ScienceDirect

Ocean Engineering

journal homepage: www.elsevier.com/locate/oceaneng

# A numerical study on the hydrodynamics of a floating tidal rotor under the combined effects of currents and waves

Federico Zilic de Arcos *, Christopher R. Vogel, Richard H.J. Willden

*University of Oxford, Engineering Department, Parks Road, Oxford, OX1 3PJ, UK*

ARTICLE INFO

*Keywords:*
Floating tidal energy
Rotor
Waves
Seakeeping
Time-domain

ABSTRACT

This work examines the hydrodynamics of a 20 m diameter axial-flow tidal rotor supported by a catamaran-style floating platform. Using a time-domain seakeeping model of the float, coupled with a dynamic model of the rotor based on blade-element momentum theory, the floating tidal turbine was analysed under the combined effects of following waves and currents. The rotor loads were analysed in scenarios with and without platform motions, starting from equivalent initial conditions. While the results show that mean power and thrust are not significantly affected, thrust and power fluctuations are substantial for the rotor under waves with and without platform motions. When platform motions were considered, amplification and reduction of load fluctuations were observed at different wave periods. These effects are associated with the phase interactions between waves and platform motion response. The reductions in thrust and power fluctuations at certain ranges of wave periods suggest that platform motions do not necessarily have an adverse impact on the operation of floating tidal rotors and could potentially be exploited to reduce fatigue damage and improve the quality of power delivery. The amplification of transient loads, on the contrary, suggests that consideration is required when designing floating systems to avoid potentially damaging effects.

## 1. Introduction

Tidal stream energy is a renewable and predictable energy source for which pre-commercial energy converters have been designed and deployed at sea (e.g., Orbital Marine Power (2021), Magallanes Renovables (2021), Andritz Hydro Hammerfest (2021) and Atlantis Resources (2021)). These devices, typically axial-flow rotors, are supported either from floating platforms, with translational and/or rotational degrees of freedom, or seabed-mounted structures such as towers with no translational nor rotational degrees of freedom.

Floating tidal energy converters have some advantages over bottom-fixed devices. These include access to faster currents near the free surface, and easier installation and maintenance, which could contribute to reducing the Levelised Cost of Energy (LCOE) of tidal stream energy. Floating devices also enable installation in deep-water locations, where bottom-fixed foundations are not feasible (Brown et al., 2021). However, there are significant challenges associated with operating floating rotors close to the free surface in marine environments. Many of these are related to environmental loads (Adcock et al., 2021).

Floating devices have been explored by industry through the development of pilot projects of commercial-scale devices (see, e.g., Magallanes Renovables (2021) and Orbital Marine Power (2021)). The complex and coupled effects of waves and platform motions are likely to play a significant role in the blade loads of floating tidal devices, and merit further investigation.

Both bottom-fixed and floating tidal rotors deployed at sea are likely to be affected by significant load fluctuations caused by transient flow phenomena (Adcock et al., 2021). Time-varying tidal currents, turbulence, shear and surface waves induce load fluctuations in rotor blades that are likely to drive maximum and fatigue loads. Turbulence and waves have been described by Scarlett et al. (2019) to be the largest drivers of unsteady loads for a bottom-fixed rotor, but their extent and influence are highly dependent on the design of a specific device and deployment location.

Typical turbulence intensity levels are in the range of 6% to 15% for sites with promising potential for tidal stream energy generation (Guerra et al., 2017; Milne et al., 2013, 2016a; Thomson et al., 2012), with length scales in the order of 10 to 14 m for a typical rotor hub height (Milne et al., 2016b; Wimshurst and Willden, 2016). The impact of high levels of turbulence on blade loads is significant. For example, Fernandez-Rodriguez et al. (2014) showed turbulence to induce load fluctuations that were 1.59 times the average thrust. Milne et al. (2016b) showed turbulence to induce blade root bending moments that can exceed the steady values by 25%, and Blackmore et al. (2016) showed fluctuations in the order of 10% to 15% of mean power

* Correspondence to: Université Le Havre Normandie, France
*E-mail addresses:* federico.zilic@univ-lehavre.fr, federico.zilic@eng.ox.ac.uk (F. Zilic de Arcos).

https://doi.org/10.1016/j.oceaneng.2023.115612
Received 26 January 2023; Received in revised form 1 August 2023; Accepted 11 August 2023
Available online 27 August 2023

and thrust, with individual blade load fluctuations in the range of 18% to 55% for the flapwise and edgewise components, respectively, for a turbulence intensity of 14.3%.

Waves are, potentially, a larger driver of unsteady loads on rotor blades. Multiple authors have found, through experiments, that mean thrust and power are not significantly affected by surface waves (e.g., Barltrop et al. (2007), Faudot and Dahlhaug (2012), de Jesus Henriques et al. (2014), Guo et al. (2018a) and Watanabe et al. (2023)). There is, however, a consensus that wave-induced load fluctuations are substantial. For example, Galloway et al. (2014) showed fluctuations of up to 175% of the median flapwise root bending moment on a blade; and Draycott et al. (2019) observed peak values in the range of 7% to 65% and 13% to 160% for thrust and power, respectively, compared with current-only cases. Wave loads depend on many factors, including incidence angle, wave amplitude, frequency, and the distance between the rotor and the free surface (Kolekar et al., 2019; Guo et al., 2018a). Thus, the intensity of these fluctuations is likely to be case-specific, but with effects that are expected to be more significant for devices operating close to the surface.

Floating tidal devices are allowed to move in different degrees of freedom, three of which are typically self-restoring and constrained by the hydrostatics of the platform (heave, pitch, and roll). The remaining three degrees of freedom (surge, sway, and yaw) are typically restrained by mooring lines or other station-keeping devices. As a consequence, floating tidal rotors operating in waves are affected by the flow fluctuations (i.e., wave kinematics) and by the motions of the floating system in response to the environmental excitation.

The motion of a rotor in some of these degrees of freedom, decoupled from waves, has been studied through the simulation of rotors under prescribed motions. Osman et al. (2019), Osman and Willden (2020), for example, studied a tidal rotor under prescribed surge and pendular motions, respectively, using Reynolds-Averaged Navier Stokes (RANS) CFD simulations. Similar to the cases above of rotors under the influence of surface waves, the studies on prescribed motions demonstrated that mean loads are largely unaffected as long as no significant flow separation is observed on the blades. However, significant load fluctuations caused by prescribed motions were described to be, potentially, in the same order of magnitude as those described by other authors for rotors in waves.

Despite the substantial literature on the effects of surface waves and the effects of prescribed motions, research on the interactions of waves and motions on floating tidal platforms is limited. These interactions can be separated into two different categories: force–motion interactions, and hydrodynamic interactions. The force–motion interactions correspond to the mechanical coupling that occurs between the rotor and the platform operating as a rigid body.

In a dynamic condition, where the environmental forces (currents, shear, turbulence, and waves) induce transient loads and motions on both platform and rotor, the force–motion interactions become increasingly complex. The motions of the platform in response to the elements can significantly affect the rotor loads by changing the flow speed relative to the blades, which adds to the underlying flow fluctuations caused by waves and other sources of unsteadiness. The changing loads on the rotor can also affect platform motion response. An example of this is the reduction of rigid-body angular motions achieved through rotor control in floating wind turbines (Skaare et al., 2015).

The hydrodynamic interactions correspond to the effects of flow changes induced by one element of the system (e.g., the floater) onto another (e.g., the rotor). While these can be significant in specific cases, (e.g., when a diffuser is placed around a rotor Tampier et al., 2017), relevant experience suggests that even large structures in proximity to a rotor can have a limited impact. Ettema (2022), e.g., evaluated a tidal fence of four rotors through towing tank experiments (using the towing tank wall as a symmetry plane) with a vertical side wall constructed with a profile-shaped cross-section. The wall was placed on one end of the fence to reduce power losses on the outboard rotor. Despite the wall having a dimension of 1.67 diameters from the free surface, only marginal changes in power and thrust were observed. McNaughton et al. (2023) evaluated, also through towing tank experiments, the effects of inter-rotor spacing in a turbine fence. Their results showed a performance uplift of up to 2.8% with an attendant increase in thrust of 1.8% by reducing the inter-rotor spacing from 1.0 to 0.25 rotor diameters. These examples suggest that the hydrodynamic interactions between a rotor and a floating platform, with a relatively low submerged volume, should be limited.

The experimental campaign of Brown et al. (2021) is one of the most comprehensive studies to date on floating tidal energy devices, to the best of the authors' knowledge. Brown et al. (2021) performed experiments on a catamaran-style platform with a porous disc mimicking a rotor. Their tests were carried under various combinations of waves and currents demonstrating, once again, that mean loads are largely unaffected by the coupled effects of waves and currents. However, they also observed amplification of unsteady loads in some of the cases where the platform motions were coupled with waves, especially at frequencies close to the pitch natural frequency.

On the numerical side, Guo et al. (2018b) studied the impact of waves and prescribed motions on a tidal rotor. The motions on a floating platform, for irregular sea states, were pre-calculated using a seakeeping time-domain model based on Cummins' equation (Cummins, 1962). These motions were then prescribed on a dynamic Blade-Element Momentum (BEM) representation of a tidal rotor (a modification of the dynamic BEM model of Hansen and Johansen (2004), and validated for a rotor in waves by Guo et al. (2018a)) that considered wave kinematics. Despite their model not considering the interactions between rotor forces and platform motion response, their decoupled analysis showed a preponderance of motion-induced load fluctuations over wave-induced. However, their analysis also showed load attenuation effects for a range of wave frequencies they associated with the pitch motion and attributed the effect to the positioning of the tidal turbine relative to the float.

More recent publications have considered the combined, although decoupled effects of prescribed motions and waves on tidal turbines. Huang et al. (2022) and Wang et al. (2022) studied tidal rotors undergoing prescribed heave and pitch motions, respectively, in the presence of regular waves. Both studies used CFD simulations and considered prescribed harmonic motions, showing significant force and power fluctuations. Wang et al. (2022) also indicates that pitch motions and waves did not significantly affect mean thrust and power. Despite their use of CFD models, these two studies did not consider the coupled dynamic response of a platform–rotor system, or the impact of the phase between the prescribed motions and the passing waves, thus difficulting the assessment of their results.

The opposite findings in terms of load amplification and load attenuation related to the pitch motion of a floating tidal rotor in waves, as described by Brown et al. (2021) and Guo et al. (2018a), are further explored in this study.

In this work, we used an engineering model to study the interactions between a tidal rotor and a floating platform. The numerical model was constructed by coupling a dynamic Blade-Element Momentum model with a time-domain seakeeping model for the float. This coupled model only considers the force–motion interactions between the rotor and the floating platform, assumed as the dominant form of interaction. The model accounts for the rotor impact on platform motion response, as well as for the impact of the platform motions on turbine forces and power performance. Despite their limited use for floating tidal energy, similar models are a robust and validated technique used both in industry and academia to study floating wind rotors (see, e.g., Jonkman and Buhl (2007) or Driscoll et al. (2016)).

The numerical model was used to analyse a conceptual design of a 70 m length double-hulled floating platform carrying a 20 m diameter tidal rotor, simulated under the combined effect of waves and currents. The ultimate goal of this study is to assess the impact of combined waves and platform response on rotor loads, and identify the causes for the load reduction and amplification effects previously described in literature.

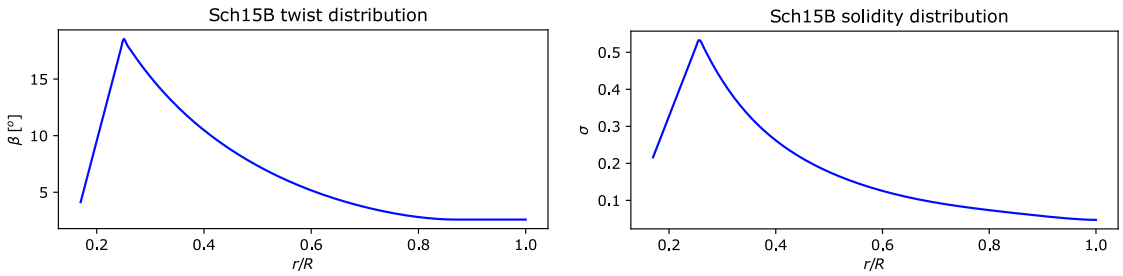


**Fig. 1.** Spanwise distribution of twist (left) and solidity (right) for the Sch15B rotor.

## 2. Methods

### 2.1. Floating system design

#### 2.1.1. Rotor

A 20 m axial-flow tidal rotor designed originally by Schluntz and Willden (2015) was used in this study. This is a three-bladed tidal rotor optimised to operate at a blockage ratio (defined as the ratio of rotor swept area to channel cross sectional area) of 19.7%. The rotor consists of a single Risø-A1-24 foil section that spans from $r/R = 0.25$, where $r/R$ is the radial coordinate $r$ normalised by the rotor radius $R$, up to $r/R = 1.0$. The sections inboard of $r/R = 0.25$ near the nacelle are linearly transitioned from a cylindrical cross section at the nacelle interface ($r/R = 0.14$) to the foil section at $r/R = 0.25$. The spanwise distribution of twist, $\beta$, and solidity, $\sigma = cN/(2\pi r)$, where $c$ is the local chord, and $N$ the number of blades, can be seen in Fig. 1.

#### 2.1.2. Floating platform

A conceptual floating system was designed to support the Sch15B rotor. The design consists of a 70 m length multi-hull platform designed as a generic and modular support structure to enable the study of floating tidal devices in single- and multi-rotor configurations. In this study a single-rotor double-hull platform is used, illustrated in Fig. 2.

The platform was designed to allow a maximum static trim angle of 1.5° when the rotor operates at the cut-out speed ($V_\infty = 4.5$ m/s). The turbine mass was estimated at 150 000 kg, and its displaced volume of 90 m$^3$ was calculated from the CAD model. The displacement, including float and rotor, was calculated to be 492 m$^3$. This estimate follows from assuming a steel hull with a plating thickness of 7 mm, following the classification rules for the design of offshore steel structures (Det Norske Veritas (DNV), 2015). A factor of 1.7 was applied to the plating mass estimate to account for other structural elements and the onboard equipment. The resulting total displacement is comparable to, e.g., Orbital's O2 reported displacement of 600 m$^3$ (Orbital Marine Power, 2021) for a single-hulled platform with two 20 m diameter rotors.

The vertical position of the centre of mass and centre of buoyancy are located at 3.2 m and 3.0 m below the waterline respectively, measured from the free surface. The roll and pitch radii of gyration of the float were assumed to be 40% of the platform's beam and 25% of its length, respectively, following the recommendations from ITTC (2017). The rotor mass inertia was estimated by assuming a homogeneously distributed mass across the nacelle. The effect of the mass distribution of the blades was deemed to be small compared with the rest of the system and was thus neglected. Note that moorings were not considered in this study, as discussed in Section 2.3. Consequently, moorings are not included as part of this floating system design.

The characteristics of the floating platform used in the computations are summarised in Table 1, and a render of the conceptual design is shown in Fig. 2.

### 2.2. Numerical models

#### 2.2.1. Rotor model

The BEM-based dynamic model of Hansen (2008) was implemented to model the tidal rotor, including the modifications of Guo et al. (2018a) to account for surface wave kinematics and added mass forces. Further modifications were included and verified to account for rotor motions, as described below.

This time-domain model works by discretising the rotor blades into a series of sections over the span, as in typical BEM models. However, the position of each of these points is tracked over time, and local flow velocities (including wave kinematics and platform motions) are resolved for each time step at each blade location. The momentum equation is then solved not over an entire annular section, as in traditional BEM, but over the fraction of the annulus that corresponds to the blade section for which forces are being calculated (one-third of the annulus for a three-bladed rotor).

The rotor-induced velocities are resolved in time using the dynamic inflow model of Øye (1991). This engineering model introduces a time delay between inflow changes and the settling of the system on a new hydrodynamic equilibrium, which is defined by a steady-state BEM solution. The model enforces the time delay on the induced velocities through two coupled first-order differential equations based on empirical constants, as described by Hansen (2008).

At a blade scale, the dynamic BEM model models dynamic stall phenomena by correcting the lift coefficients for trailing edge separation, considered to be the dominant separation phenomenon for axial-flow rotors by Hansen et al. (2004). This model, similar to the dynamic inflow model, uses a first-order differential equation to introduce a time lag. The delay is applied not to the induced velocities, however, but to a flow separation function.

The separation function is a description of the percentage of the chord of a foil where the flow is separated. The lift coefficients are related to this function by assuming that the lift at any time is a linear combination of the coefficients corresponding to the fully-attached and fully-separated flow regimes. The proportion of lift corresponding to each regime at any given time is defined by the separation function. By applying the differential equation to the separation function, the model introduces a time delay for flow separation and reattachment, enabling the calculation of a time-dependent lift coefficient, and modelling the stall delay and hysteresis normally observed for oscillating aerofoils. Further details are given by Hansen et al. (2004), Hansen (2008), and Zilic de Arcos (2021).

Guo et al. (2018a) introduced two modifications to this dynamic BEM model: wave kinematics through the use of first-order wave theory, and added-mass forces considered through the inertial component of Morison's equation (Morison et al., 1950). Their model was validated against an extensive campaign of tank experiments, performed by the authors, on a 1:25 scaled tidal rotor. Their numerical results showed a good agreement with their experimental results in terms of average and unsteady loads across a broad range of waves, currents, and nacelle submergence depths.

**Table 1**
Principal characteristics of the conceptual floating tidal platform designed for this study.

| Description | Value | Unit | Description | Value | Unit |
|---|---|---|---|---|---|
| Total displaced volume | 492.0 | [$m^3$] | Waterplane area | 519.5 | [$m^2$] |
| Total displacement | 504 036.0 | [kg] | Vertical centre of mass | −3.2 | [m] |
| Total length | 70.0 | [m] | Vertical centre of buoyancy | −3.0 | [m] |
| Beam overall | 30.0 | [m] | Metacentric height (roll) | 179.9 | [m] |
| Beam demi-hull | 4.0 | [m] | Metacentric height (pitch) | 386.13 | [m] |
| Maximum draft | 25.0 | [m] | Heave natural frequency | 0.262 | [Hz] |
| Roll inertia | 8.4E+07 | [kg $m^2$] | Roll natural frequency | 0.226 | [Hz] |
| Pitch inertia | 1.4E+08 | [kg $m^2$] | Pitch natural frequency | 0.273 | [Hz] |
| Yaw inertia | 1.1E+08 | [kg $m^2$] | | | |

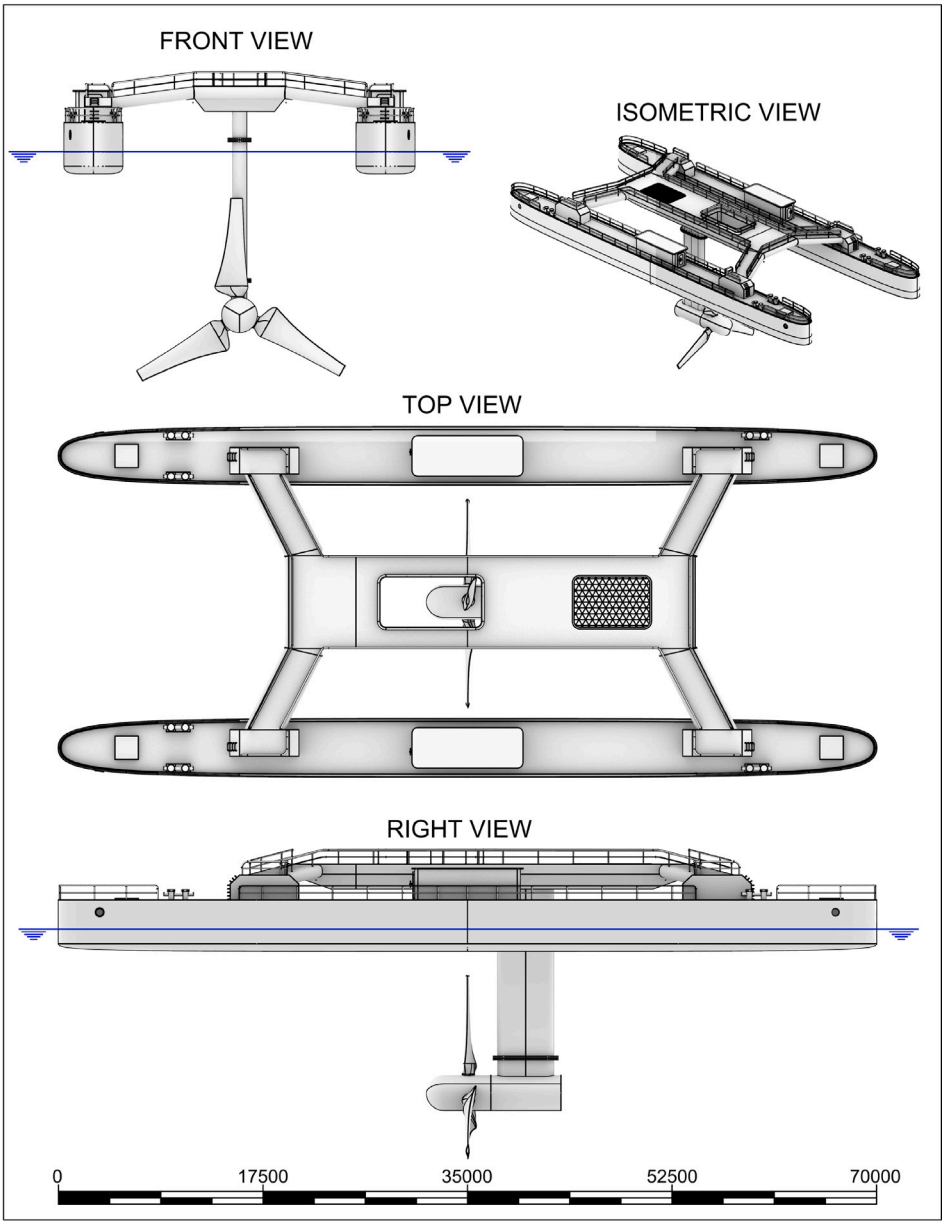


**Fig. 2.** Render of a conceptual dual-hull floating platform design for tidal stream energy applications.

In the present work, further modifications were introduced to the dynamic BEM model presented by Guo et al. (2018a). The first modification is related to the motions of a floating platform. These are accounted for by the definition of the relative motion velocity, $\vec{V}_{motion}$, on each blade section. The different velocity components are resolved in different frames of reference, and ultimately the axial and tangential velocity components, relative to the foil frame of reference shown in Fig. 3, is used in each computation. The apparent velocity is thus defined as:

$$\vec{V}_{rel} = \vec{V}_{\infty} + \vec{V}_{rot} + \vec{V}_{W} - \vec{V}_{motion} + \vec{W} \tag{1}$$

where $\vec{V}_{rel}$ is the relative flow speed as seen at an $r_i$ blade section of blade $B_i$, $\vec{V}_{\infty}$ is the undisturbed current speed, $\vec{V}_{rot}$ the rotational speed,

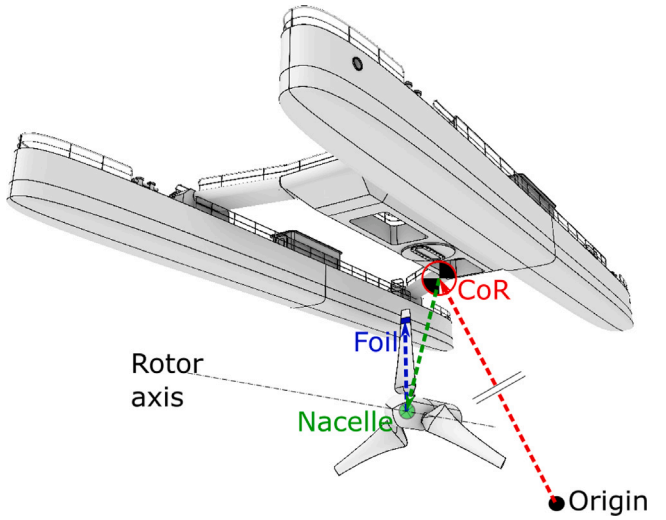


**Fig. 3.** Diagram of the different frames of reference used for the calculation of the local flow velocities at each blade section. The tower has been removed for clarity.

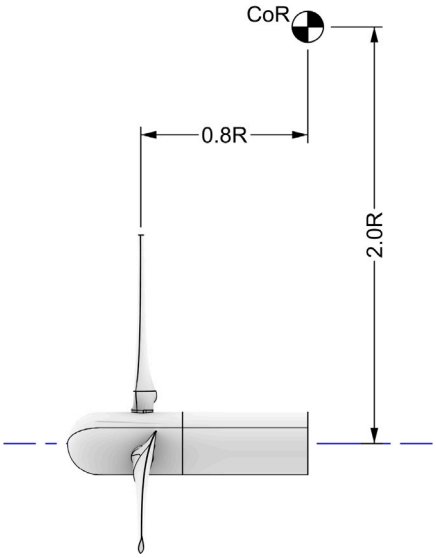


**Fig. 4.** Relative position of the rotor with respect to the Centre of Rotation (CoR) used for the pendular motion simulations described by Osman and Willden (2020).

$\vec{V}_W$ the wave induced velocity, $\vec{V}_{motion}$ the rigid body motions resolved at the blade section, and $\vec{W}$ the rotor induced velocities.

The model is completed with elements of a steady-state BEM model, which solve the steady-state values towards which the dynamic sub-models converge. The determination of the steady-state induced velocities is achieved through the single-equation derivation of the BEM equations presented by Ning (2014), including tip-loss effects that are modelled using Prandtl's tip-loss model (Prandtl, 1921). The blades were discretised with 40 points each, and we used lift and drag coefficients calculated with a RANS CFD model, with a k-$\omega$ SST turbulence closure and a Reynolds number $Re = 8.0 \times 10^6$, following the configuration presented in Zilic de Arcos et al. (2018). The Reynolds number corresponds to the mid-span average for the analysed conditions. In addition, we used a modified version of the turbulent wake model (TWM) of Buhl (2005) for high-load regimes, as described in Zilic de Arcos (2021). This modified TWM, combined with the polar coefficients, was shown to improve the predictive capabilities of the steady-state BEM computations, for the tidal rotor used in this study, across the span of the blade and at different tip-speed ratios (Zilic de Arcos, 2021).

*2.2.1.1. Model verification.* The modifications made to the dynamic BEM model to account for rotor motions were verified by comparing its predicted results with blade-resolved CFD simulations. The prescribed-motion CFD results of Osman and Willden (2020) were used for comparison. Their work describes the effects on loads and power performance that occur when the Sch15B rotor oscillates in pendular motion. This is a harmonic pitching motion, with a Centre of Rotation (CoR) located some distance from the rotor. This mode imitates the pitching motion of a floating platform and its impact in rotor blades. The frame of reference for this prescribed motion is shown in Fig. 4.

The cases simulated by Osman and Willden (2020) were reproduced using the dynamic BEM model. The results, in Fig. 5, show a comparison between the CFD and dynamic BEM results in terms of the integrated power and thrust, for different oscillation frequencies $\omega^*$, defined as the pendular motion frequency normalised by the rotational frequency of the rotor. These results demonstrate good agreement between the two numerical models, especially for lower values of $\omega^*$. Lower frequencies lead to smaller oscillations in angle of attack, and consequently place a smaller demand on the dynamic inflow and dynamic stall models.

The results of the dynamic BEM model show a maximum relative error at peak load of approximately 13%, compared with the CFD simulations, for the largest $\omega^*$, and substantially smaller error values for lower oscillation frequencies. The main sources of error are related to limitations on the tip-loss model, which leads to an overestimation of thrust and especially of power near the tip of the blade, and also to limitations on the dynamic stall model where a substantial flow separation is observed (Zilic de Arcos, 2021). However, the model predictions are considered satisfactory for cases where stall is not observed or where it only occurs over a small portion of the rotor blades. Further details and a more detailed comparison between the engineering model and the CFD results of Osman and Willden (2020) are outside the scope of this paper, but can be found in Zilic de Arcos (2021).

*2.2.2. Seakeeping model*

The time-domain hydrodynamic model of Cummins (1962) was used to model the floating platform. This seakeeping model is based on pre-computed hydrodynamic coefficients, and is expressed by the following equation of motion:

$$\{\boldsymbol{M_{RB}} + \bar{\boldsymbol{A}}(t)\}\ddot{\boldsymbol{X}}(t) + \int_{-\infty}^{t} \bar{\boldsymbol{K}}(t-\tau)\dot{\boldsymbol{X}}(\tau)d\tau + \bar{\boldsymbol{C}}\boldsymbol{X}(t) = \boldsymbol{F}_{ext}(t) \tag{2}$$

with $\boldsymbol{M_{RB}}$ the floating platform rigid-body mass matrix, $\bar{\boldsymbol{A}}(t)$ the time-domain added mass matrix, $\boldsymbol{X}$ the platform position vector, $\bar{\boldsymbol{C}}$ the stiffness matrix and $\boldsymbol{F}_{ext}$ the excitation forces, which include environmental and rotor forces.

The coefficients in Eq. (2) are determined from the hydrodynamic coefficients calculated in the frequency-domain. Ogilvie (1964) showed that, for the case of harmonic motions, Cummins' model is equivalent to a frequency-domain model. Ogilvie's transformations, thus, enable the calculation of the hydrodynamic coefficients for the time-domain model using frequency-domain hydrodynamic coefficients, with the relationship between frequency and time-domain coefficients given by:

$$\bar{\boldsymbol{A}}(t) = \boldsymbol{A}(\infty) \tag{3}$$

and

$$\bar{\boldsymbol{K}}(t) = \frac{2}{\pi}\int_0^{\infty} \boldsymbol{B_{tot}}(\omega)\cos(\omega t)d\omega \tag{4}$$

where $\boldsymbol{A}(\infty)$ is the frequency-domain added mass evaluated at the limit where $\omega \to \infty$, and $\boldsymbol{B_{tot}}$ is the frequency-domain total damping matrix.

ANSYS AQWA 19.0 was used to calculate the frequency-domain hydrodynamic coefficients and first order wave forces by describing

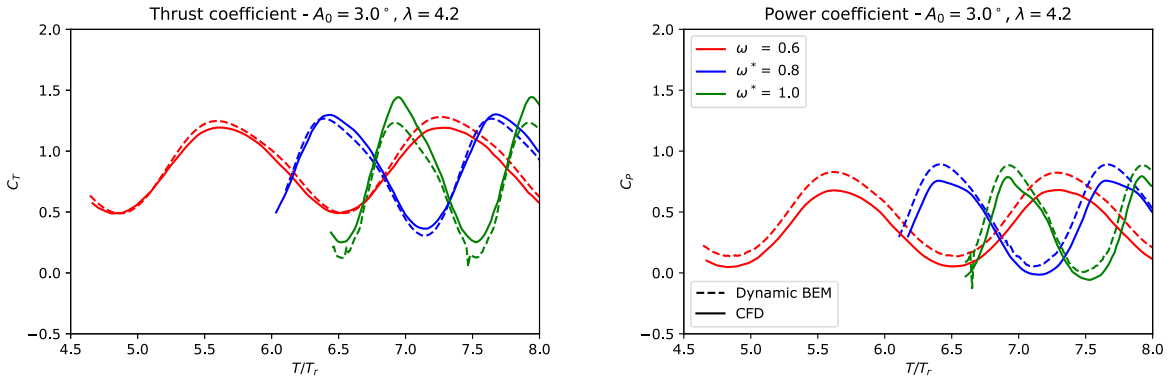


**Fig. 5.** Thrust (left) and power (right) coefficient comparison between Osman and Willden (2020) blade-resolved CFD (solid lines) and the dynamic BEM computations (dashed lines) of the Sch15B rotor under a prescribed pendular motion at varying $\omega^*$.

the flow around the float with a velocity potential. This potential is represented by the incident waves, diffraction and radiation terms. The incident forces and hydrodynamic coefficients are computed through the discretisation of the surface of the floating body into panels on which the potentials are calculated. The potentials are then used to compute the active forces from the incident wave and diffraction potentials, and the reactive forces, obtained from the radiation potentials solved for each degree of freedom. The reactive forces are finally used in the model to calculate the frequency-domain added mass and damping coefficients (ANSYS, 2018).

The rotor model is coupled with the time-domain hydrodynamic model shown in Eq. (2) through the right-hand side of the equation. The time-varying excitation forces in this model, $F_{ext}(t)$, include the wave excitation over the float along with the rotor forces obtained from the dynamic BEM model.

The time-domain model was solved with ANSYS AQWA 19.0, along with a Python implementation of the dynamic BEM model. The coupling of the two codes works through an external server connection. The dynamic BEM code receives, twice per time-step, a state vector including time, position, and velocity of the centre of gravity of the floating platform. The state vector is used by the dynamic BEM code to resolve the state of each blade element, and the relative inflow velocity. Wave kinematics are incorporated through first-order wave theory both in AQWA and the dynamic BEM model, and are synchronised in time. The dynamic BEM code calculates the rotor forces on a sectional basis, integrates them over the rotor, and returns them to AQWA as a six-component force vector. Eq. (2) is finally integrated by AQWA using a predictor–corrector approach, with the forces received from the dynamic BEM code added to the $F_{ext}(t)$ term on the right-hand side of the equation.

### 2.3. Modelling conditions

The floating platform was modelled under different combinations of waves and currents. Four different current speeds ($V_\infty \in \{1.0, 2.0, 3.0, 4.0\}$ [m/s]) were combined with 12 different regular waves of varying length, $\lambda_W \in \{35, 70, 105, 140, 175, 210, 280, 350, 420, 490, 560, 630\}$ [m], corresponding to 0.5 to 9 platform lengths. The current and waves are assumed to be aligned with the platform centre line, with waves propagating in the same direction as the current. A constant wave height of 1m is assumed, and wave periods were adjusted to account for the Doppler shift effect due to the presence of the tidal current. Waves are, thus, resolved in terms of the encounter frequency, $\omega_e$, relative to the platform:

$$\omega_e = \omega_W + kV_\infty \tag{5}$$

with $\omega_W$ the wave frequency, and $k$ the wave number. Wave lengths are related to the wave period $T_W = 2\pi/\omega_W$ by:

$$\lambda_W = \frac{g}{2\pi} T_W^2 \tanh kd \tag{6}$$

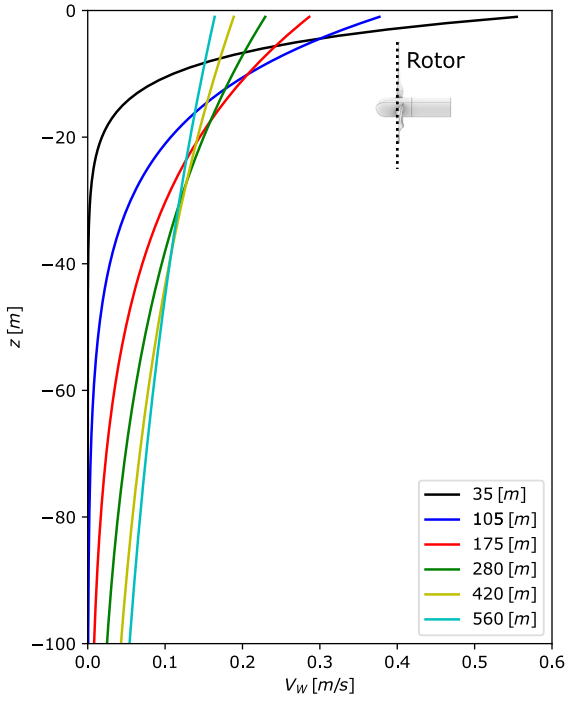


**Fig. 6.** Profile showing the amplitudes of the wave-induced velocities, as a function of depth, for different wave lengths of 1 m height. The origin is placed at the mean free surface level.

where $g$ is the gravitational acceleration, and $d$ the channel depth. Profiles of maximum wave-induced velocities, as a function of depth, are depicted in Fig. 6 for some of the analysed waves.

The platform was studied under two conditions regarding its degrees of freedom. In the first case, the platform is assumed to be restrained and not allowed to move, thus operating in a similar way to a bottom-fixed device. This configuration is referred to as the "fixed rotor" in the following sections. In the second case, referred to as the "floating rotor", the platform is allowed to move freely in heave and pitch, both of which are degrees of freedom with restoration depending on hydrostatics and, consequently, platform design. Given the assumption of aligned currents and waves, roll motions were neglected. The remaining

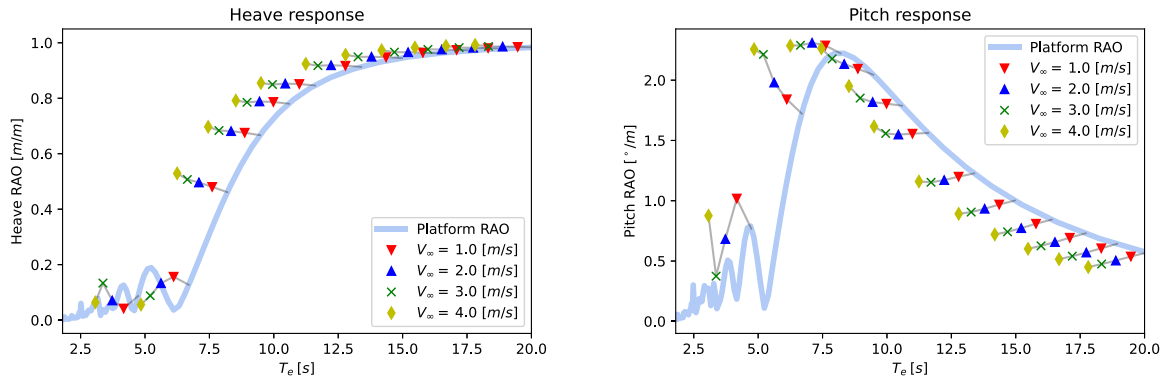


**Fig. 7.** Frequency-domain RAOs of the floating platform without the rotor (blue line) compared with the time-domain response of the platform with the rotor, as a function of encounter period $T_e$, operating at a constant tip-speed ratio $\lambda = 5.0$ and with different inflow velocities (bullets). Bullet points of different inflow velocities that correspond to equivalent wave lengths are linked by grey lines.

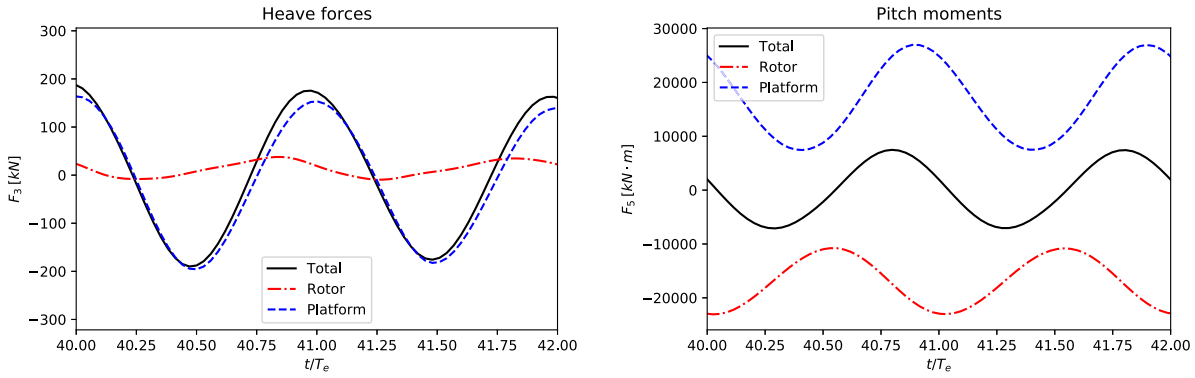


**Fig. 8.** Extract from the time series: heave forces (left) and pitch moments (right) acting on the platform and rotor at a current speed of $V_\infty = 3.0$ [m/s] and with a wave encounter period $T_e = 3.4$ [s].

degrees of freedom (surge, sway and yaw) were neglected in the model since restoration would depend on moorings or other station-keeping devices, which are beyond the scope of this work.

The modelled time-series started, both for the fixed and floating rotor configurations, from the same initial static equilibrium condition which includes the steady-state force generated by the rotor. The time series were modelled for at least 30 wave periods, using a time step of 0.1 s, and with 10 s of ramping time. The rotor was assumed to operate at a constant tip-speed ratio of $\lambda = 5.0$, with $\lambda = \omega R/V_\infty$, and $\omega$ a constant rotational speed. Initial transients in the time series were discarded at the post-processing stage.

## 3. Results

### 3.1. Impact of the rotor on platform motions

Fig. 7 shows the frequency-domain Response Amplitude Operator (RAO) of the floating platform for heave and pitch for different wave encounter periods $T_e$. These RAOs represent the ratio of motion amplitude to wave amplitude. The plots show the response calculated with AQWA in the frequency domain, compared with the different cases extracted from the time-domain simulations at different wave periods and current speeds. Note that the frequency-domain solution corresponds to the case of the platform without the effects of the hydrodynamic forces of the rotor, but is otherwise equivalent in mass and mass distribution. The continuous line represents the RAOs calculated with AQWA in the frequency domain, while the different bullet points correspond to the simulated cases with the rotor operating in different flow speeds and wave periods. Due to its design, the platform experiences significant multi-hull interactions for the shorter wave range, $T_e \leq 7.5$ s. These are made evident by the amplification and attenuation effects for both pitch and heave shown by the platform-only RAOs in Fig. 7.

The heave and pitch response plots show a small, yet non-negligible, influence of the rotor on platform response. Due to the period shift, we observe a displacement of the bullets towards lower encounter periods as flow speed increases, compared with the frequency-domain solution for the platform response without the effect of the rotor. Heave shows an increased response in the analysed range, especially at shorter encounter periods. Pitch shows an increased response for the cases with the rotor at encounter periods less than 7.5 s, and a reduction in the response above this period compared to the no-rotor case. The increased response and spread of bullets for the shorter encounter periods is attributed to the coupling between the rotor and the multi-hull platform dynamics.

The changes in pitch and heave response are caused by a combination of factors, but mainly due to the rotor inducing significant hydrodynamic forces on the system. Fig. 8 shows an example of heave forces and pitch moments on the float, rotor, and the total forces on the coupled system, for an encounter period of $T_e = 3.4$ s, and a current speed of $V_\infty = 3.0$ m/s. The figure shows the significant moments and forces that the rotor induces in both pitch and heave. Their impact, however, depends not only on the magnitude of these forces, but also on the interaction between the waves and the platform response, as discussed in the following section.

### 3.2. Rotor loads and performance

Fig. 9 shows a comparison of the mean thrust and thrust fluctuations between the floating and fixed rotors, for different waves and current conditions. The bullet points show mean quantities, while bars

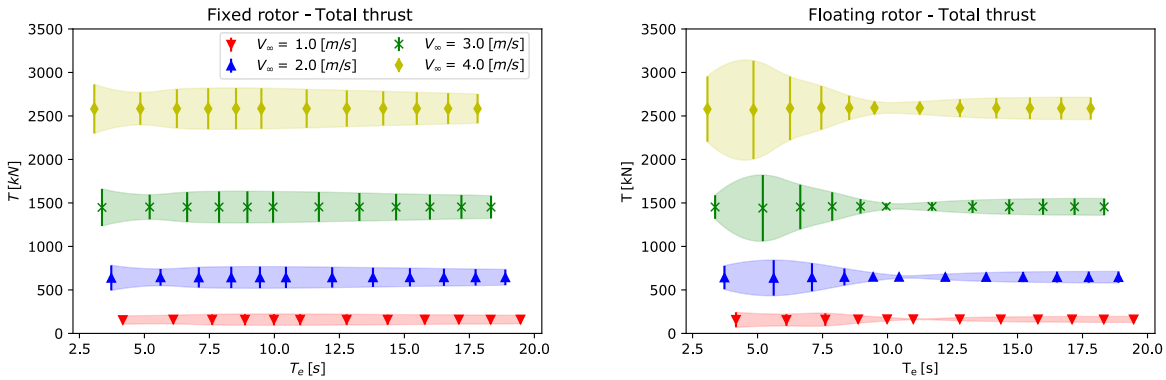


**Fig. 9.** Mean thrust (bullet points) and thrust fluctuations for the fixed (left) and floating (right) rotors as a function of encounter period for different inflow speeds. The thrust fluctuations are represented by two standard deviations (vertical bars and shaded areas).

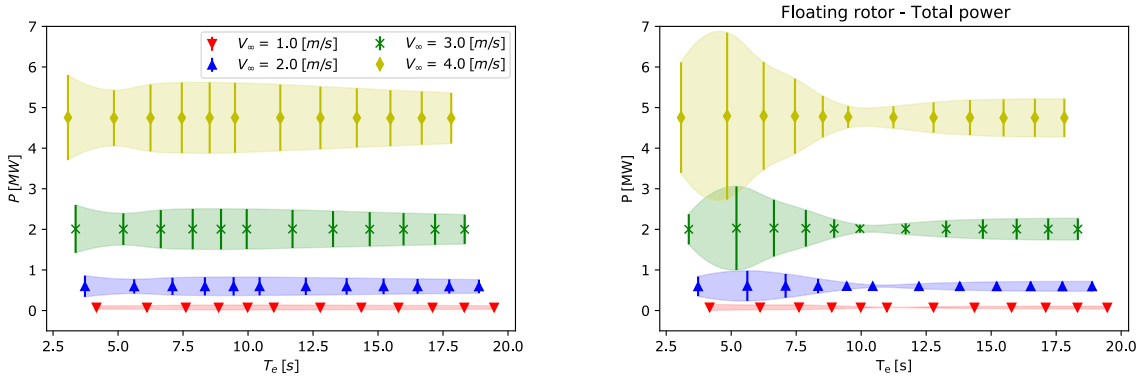


**Fig. 10.** Mean power (bullet points) and power fluctuations for the fixed (left) and floating (right) rotors as a function of encounter period for different inflow speeds. The power fluctuations are represented by two standard deviations (vertical bars and shaded areas).

and shaded areas show load fluctuations represented by two standard deviations.

The thrust plots show that mean values are not significantly influenced by waves nor by platform motions. This is in agreement with the results presented by, e.g., Galloway et al. (2014), de Jesus Henriques et al. (2014), and Guo et al. (2018a), for cases of rotors operating under the influence of surface waves, and by Osman and Willden (2020) and Osman et al. (2019) for rotors under prescribed motions. The load fluctuation magnitude, however, varies between cases as a function of wave period. At relatively low encounter periods, and for all current speeds, our results show larger load fluctuations for the floating rotor than for the fixed device. The trend is inverted for longer waves, however, where the floating rotor shows smaller load fluctuations. For the floating device, with a wave encounter period of approximately $T_e = 10 - 12$ s, all current speeds show a significant reduction in the thrust fluctuations. Note that all these trends are similar for the integrated power, as shown in Fig. 10.

The relatively larger load fluctuations for a floating rotor compared with a fixed device has been observed experimentally by Brown et al. (2021), and they suggested those occurred at frequencies close to the pitch natural frequency of their platform. Similarly, the numerical model of Guo et al. (2018b) also predicted larger thrust fluctuations for a floating rotor compared with a fixed device in irregular sea states. The load amplification at low wave periods can be related to the discussion on the RAOs and the apparent displacement of the pitch peak response towards lower encounter periods, which suggests a preponderance of motion-induced velocities in this low period range. However, the reduced load fluctuations observed at higher wave periods cannot be directly explained through platform motions.

Fig. 11 shows that the heave and pitch motion do not exhibit any abrupt changes in behaviour around the wave encounter periods where transient load attenuation is observed, neither in terms of mean nor fluctuating components. It follows that the reduction in load fluctuations does not occur due to the magnitude of platform motions, but due to the relative phase between the waves and the platform response.

Fig. 12 shows the axial component of flow velocity, relative to a blade section located at $r/R = 0.75$, for two different wave conditions. The plot on the left corresponds to an encounter period where we observe the amplification of transient loads ($T_e = 3.7$ s), while the plot on the right is within the region of significant transient load reductions ($T_e = 12.2$ s). The plots show three different curves: the motion-induced velocities that occur as a consequence of platform motion, the wave-induced velocities as sampled by the foil section as the blade rotates, and the net inflow velocity fluctuations, which corresponds to the sum of the aforementioned components.

The plots in Fig. 12 highlight that, for the load-amplification case, the velocity fluctuations are dominated by the motion-induced component. In this case, not only is the net inflow dominated by the platform motion but also the similar phase of the platform motions and wave kinematics mean that there is constructive interaction between the two components, resulting in an amplification of the velocity fluctuations seen by the blade. On the contrary, for the case of abrupt transient load reduction, we observe that both wave- and motion-induced velocities have a similar magnitude. Their relative phase, however, is such that the resulting net inflow is diminished, leading to the load reduction previously observed. Ultimately, we observe that the magnitude and phase interactions between wave kinematics and motion-induced velocities is what, ultimately, drives the amplification or attenuation of thrust and power fluctuations.

The trends in rotor thrust and power can be assessed through the impact of wave- and motion-induced velocities on the angle of attack on a representative blade section. The mean and fluctuating components

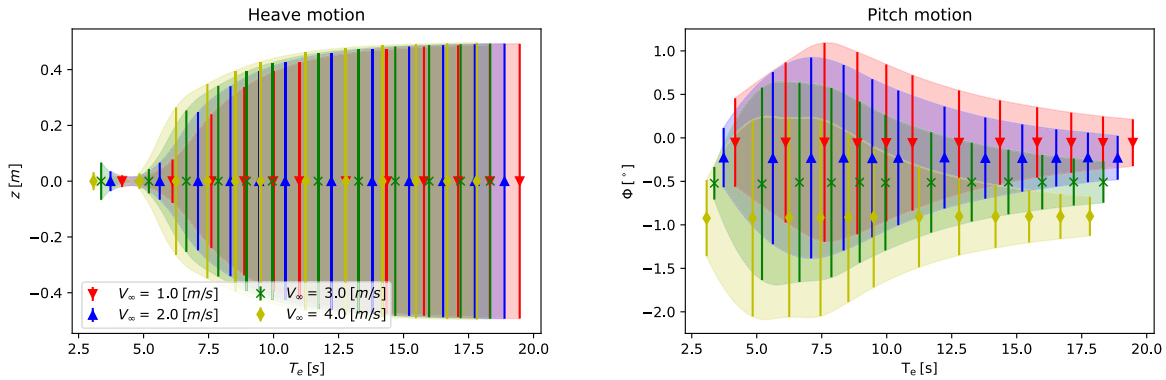


**Fig. 11.** Mean and oscillatory fluctuations of heave (left) and pitch (right) motions for the floating platform with rotor as a function of encounter period for different inflow speeds. The motion fluctuations are represented by two standard deviations (vertical bars and shaded areas).

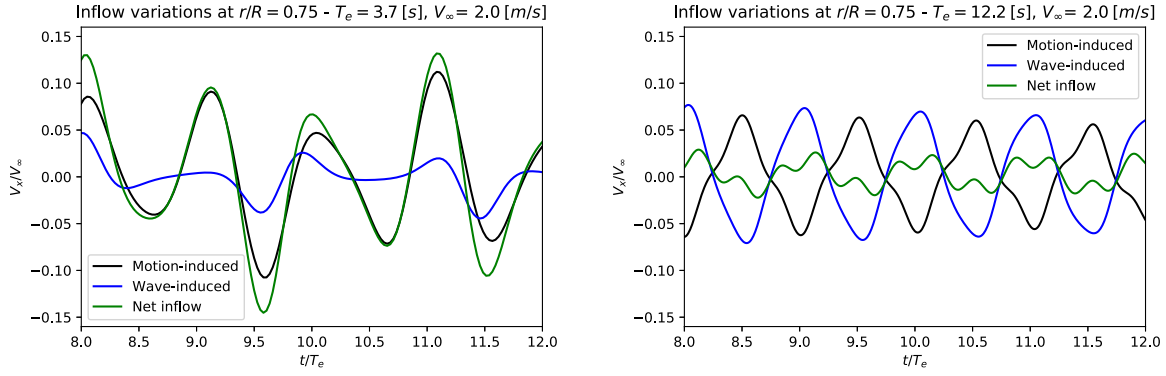


**Fig. 12.** Axial inflow speed variations at $r/R = 0.75$ for a floating rotor operating at $V_\infty = 2.0$ [m/s] at two different wave encounter periods. The plots show the net inflow fluctuations alongside the wave- and motion-induced velocities. Note that only the velocity fluctuations, and not the mean current, are shown.

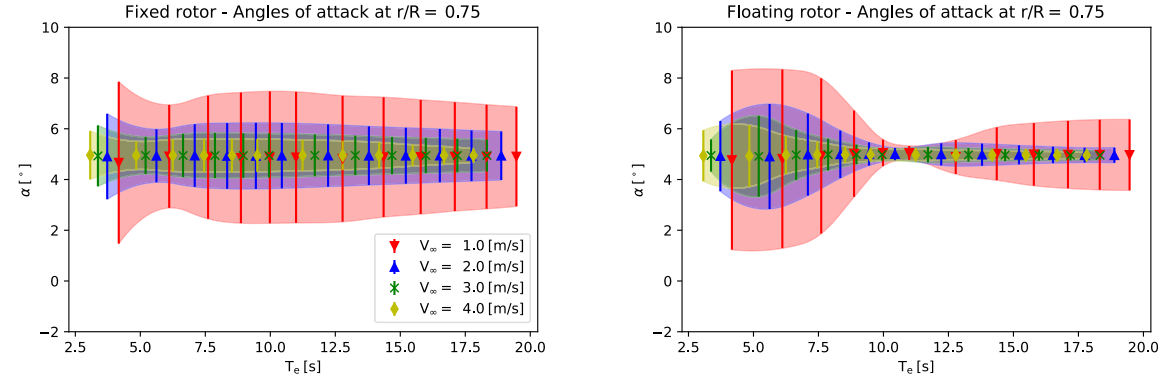


**Fig. 13.** Mean angle of attack (bullet points) and thrust fluctuations at $r/R = 0.75$ for the fixed (left) and floating (right) rotors as a function of encounter period for different inflow speeds. The thrust fluctuations are represented by two standard deviations (vertical bars and shaded areas).

of the angle of attack, presented for a blade section at $r/R = 0.75$ in Fig. 13, reflect the interactions between waves and platform motions. Similar to the thrust and power plots, this figure shows little change in the mean angle of attack, and highlights that the load amplification and attenuation at low and high encounter periods, respectively, are associated with corresponding fluctuations in angle of attack.

It is interesting that for longer waves, smaller fluctuations in angle of attack are observed for the floating rotor compared with the fixed device. This occurs because, for longer excitation periods, the platform motion starts approaching a quasi-static response in phase with the waves. The floating platform passively moves in the direction of the loads, reducing the relative velocity perturbations seen by the blades and, ultimately, resulting in smaller load and angle of attack fluctuations due to the platform compliance.

The preponderance of platform motion- and wave-induced velocities also drive changes in the distribution of transient loads over the azimuth. Fig. 14 shows the azimuthal distribution of thrust, for one blade, for the fixed rotor. The figure depicts two different wave periods, located below and above the zone of abrupt load attenuation for the floating rotor. The continuous line shows the mean thrust, while the shaded area represents the transient fluctuations, measured by two standard deviations, at each azimuthal location. Similar to the

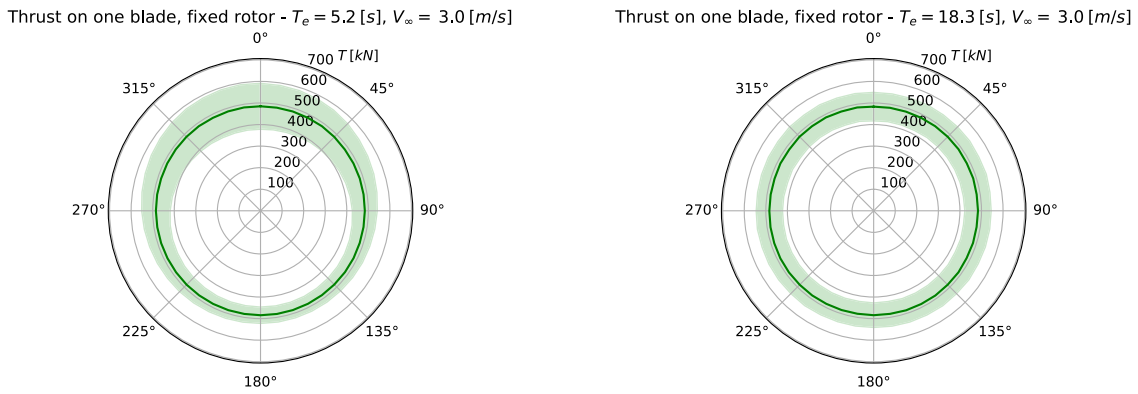


**Fig. 14.** Azimuthal distribution of thrust on a single blade of a fixed rotor. The plot shows the mean thrust (solid line) and two standard deviations of the oscillatory component (shaded area). The two plots present the rotor operating at different encounter periods, $T_e = 5.2$ [s] (left) and $T_e = 18.3$ [s] (right), at a current speed $V_\infty = 3.0$ [m/s]. 0° corresponds to the top dead centre.

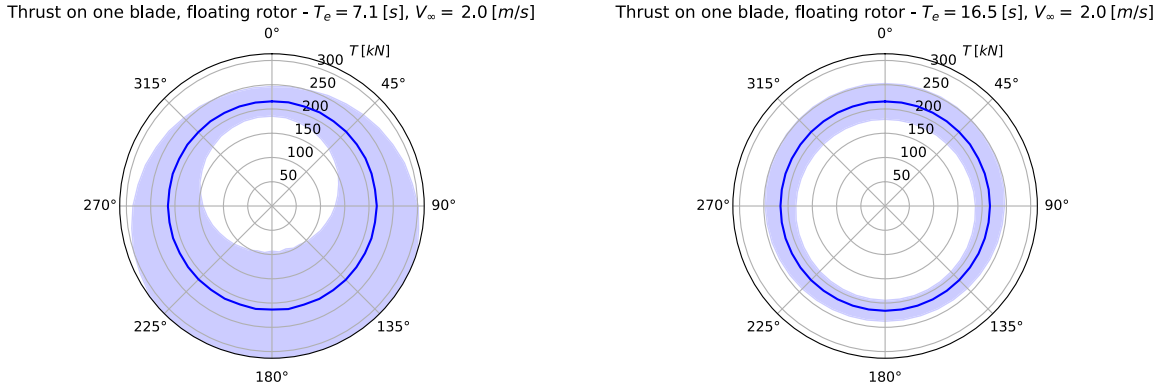


**Fig. 15.** Azimuthal distribution of thrust on a single blade of a floating rotor. The plot shows the mean thrust (solid line) and two standard deviations of the oscillatory component (shaded area). The two plots present the rotor operating at different encounter periods, $T_e = 7.1$ [s] (left) and $T_e = 16.5$ [s] (right), at a current speed $V_\infty = 2.0$ [m/s]. 0° corresponds to the top dead centre.

integrated loads in Figs. 9 and 10, these plots show no azimuthal variations in the mean load. Azimuthal variations in the load fluctuations are observed, concentrated near the free surface for the shorter wave ($T_e = 5.2$ s), while they are more homogeneously distributed over the entire azimuth for the higher encounter period ($T_e = 18.3$ s). This is a consequence of wave kinematics decaying more abruptly with depth for shorter period waves, as shown in Fig. 6.

Fig. 15 shows the azimuthal distribution of thrust for two cases on the floating rotor, one at an encounter period below the abrupt load reduction region ($T_e = 7.1$ s) and one of a longer period ($T_e = 16.5$ s). As before, no significant azimuthal variation is observed for the mean thrust. However, for the shorter wave, the largest load fluctuations are concentrated near the bottom dead centre (blade position) as a consequence of the dominance of the motion-induced velocities. The apparent speed caused by significant pitch motions, as shown in Fig. 11, is maximised at the farthest location from the centre of rotation, thus producing larger thrust fluctuations at the bottom dead centre. On the contrary, transient loads are slightly more concentrated near the free surface for the longer wave, with a bottom-to-top transition in the azimuthal position where the largest fluctuations occur around the range of periods where the abrupt reduction of transient loads is observed.

## 4. Discussion

The floating rotor, unlike the fixed device, showed significant changes in the amplitude of load fluctuations with wave period. Three different phenomena when comparing the floating with the fixed device were observed across the range of wave periods analysed: a transient load amplification at short wave periods, a region of abrupt reduction of transient loads for periods in the range of 11 to 12 s, and a region where load fluctuations are slightly reduced for the longer waves.

The region of transient load reductions at an encounter period of approximately 11 s was demonstrated to occur at a frequency range where wave- and motion-induced velocity fluctuations on the blades were of similar magnitude but, due to their relative phase, tend to negate each other. This observation suggests that platform motions, often considered to be an undesirable effect, could be used to significantly reduce power and thrust fluctuations on a floating tidal device for specific periods of following waves. The specific range of frequencies where the load fluctuations are reduced depends on platform design and rotor response, and further studies are required to determine whether this phenomenon could be exploited from the design of floating systems for practical purposes.

The effect of the phase between waves and motions on blade loads is consistent with some of the results presented by Guo et al. (2018b), where they compare a rotor under equivalent prescribed motions (obtained from the time-domain simulation of a floating platform decoupled from the rotor) with and without considering the influence of following wave kinematics on blade loads. Specifically, they describe a reduction in thrust fluctuations at certain wave frequencies, which they relate to the longitudinal position of the rotor. This explanation corresponds to the concept of phase between motions- and wave kinematics also observed in our work. By changing the distance between the rotor and the centre of rotation, Guo et al. (2018b) affected the time-delay between platform response and the waves reaching the rotor. However, in addition to their conclusions, we consider that the phase difference between waves and motion response is also a function of

platform design and its interaction with the rotor. Factors like rotor design and operation, as well as float shape and mass distribution are likely to influence the motion response, amplitude and phase, potentially to a greater extent than the relative position of the rotor.

Our modelled results, however, are to be regarded as an initial exploratory analysis upon which further work is required. In particular, the assumption of regular and following waves only correspond to a small subset of cases amongst the range of conditions a device might encounter in its operational life. Irregular waves with different propagating directions, and exciting all six degrees of freedom, are likely to induce effects not considered in this study. The extension of the analysis conditions, however, to specific cases such as beam seas and rotor misalignment, might also require further corrections and validation of the dynamic BEM model.

The study faces uncertainty associated with the limitations of the numerical model. The uncertainty regarding the physics being modelled was reduced by the verification of the dynamic BEM model, by the extensive validation done by Guo et al. (2018a), and by selecting analysis cases where the model can operate within the boundaries where its validity is considered sufficient, i.e., where no significant flow separation occurs. Specifically, and as shown in the discussion on the angle of attack, the rotor was operating mostly below the static stalling angle for the Risø-A1-24 foil ($\alpha \approx 11°$) for most cases.

However, the largest source of uncertainty in this work is related to fluid dynamic effects not included in our engineering model. The rotor model does not consider hydrodynamic interactions with the platform or with the free surface, which have been shown to be significant (see, e.g., Brown et al. (2021) and Kolekar et al. (2019)) although of lesser importance than the force–motion interactions described in this study. Amongst other things, these hydrodynamic interactions are likely to affect the azimuthal symmetry of mean thrust seen in this study. Wave diffraction effects caused by the rotor, which are potentially relevant for the platform response, are also neglected in the numerical model, and further work is required to determine their relevance. Finally, and despite not affecting blade loads significantly (Guo et al., 2018a), added mass is likely to have an impact on the floating platform motion response, as shown in the discussion about the heave and pitch RAOs. Added mass, in particular, is included in the dynamic BEM model under a flat-plate simplified assumption based on the inertial term of Morison's equation (Morison et al., 1950), which ought to be tested in more detail. All these areas require further studies developed using higher-fidelity numerical models and/or controlled experiments.

## 5. Conclusions

The results obtained in this work show three interesting phenomena for floating tidal rotors operating in regular following waves. First, it supports the findings of previous research that mean thrust and power should not be significantly affected by whether a rotor is floating or attached to a fixed support structure, for the range of current speeds, wave height, and wave frequencies analysed. Second, the numerical model predicts significant oscillations in thrust, power, and angle of attack for both fixed and floating rotors. The observed fluctuations, however, were not necessarily larger for the floating device for all wave periods. Third, the amplitude and phase interactions between wave kinematics and platform motion response, influenced by platform design, play a key role in the amplification or reduction of load fluctuations for floating devices.

The identification of three operational zones where load fluctuations are amplified, significantly reduced, and mildly reduced for a floating device agrees with some of the observations made by Brown et al. (2021) and Guo et al. (2018b). Our work, however, contributes to the state of the art by describing the hydrodynamic mechanisms that cause these effects in rotor loads, and identifies, through the use of a time-domain engineering model that couples rotor and platform dynamics, that the phase between wave-induced kinematics and platform–rotor coupled motion response is a critical parameter for transient load amplification or attenuation on floating tidal rotors.

The availability of high-fidelity CFD models notwithstanding, engineering models are likely to play a significant role in the analysis and design of offshore devices, where large number of cases and time-series make high-fidelity CFD simulations prohibitive. The implementation, modification, and verification of the numerical model used in this study, based on observations made from higher-fidelity simulations, has enabled the analysis of a range of current and wave conditions for fixed and floating tidal rotors, highlighting interesting phenomena and establishing potential areas for future research that could contribute towards the development of cost-competitive renewable energies.

Future work will be aimed at developing higher-fidelity models capable of capturing some of the physics neglected in this work, and at reducing the modelling uncertainty of the engineering tools used for the study of floating tidal devices.

## CRediT authorship contribution statement

**Federico Zilic de Arcos:** Conceptualization, Methodology, Software, Formal analysis, Investigation, Data curation, Resources, Writing – original draft. **Christopher R. Vogel:** Conceptualization, Methodology, Formal analysis, Resources, Supervision, Writing – review & editing. **Richard H.J. Willden:** Conceptualization, Supervision, Writing – review & editing.

## Declaration of competing interest

The authors declare that they have no known competing financial interests or personal relationships that could have appeared to influence the work reported in this paper.

## Data availability

Data will be made available on request.

## Acknowledgements

This research project was supported in part by CONICYT PFCHA/BECAS CHILE DOCTORADO EN EL EXTRANJERO, Chile 2016/72 170292. This project also received funding from the European Union's Horizon 2020 research and innovation programme under the Marie Skłodowska-Curie grant agreement No 101034329, recipient of the WINNINGNormandy Program supported by the Normandy Region. RHJW would like to acknowledge EPSRC, UK who support his fellowship through grant number EP/R007322/1. CRV acknowledges the support of the UKRI, UK through his Future Leaders Fellowship MR/V02504X/1.

## References

Adcock, T.A.A., Draper, S., Willden, R.H.J., Vogel, C.R., 2021. The fluid mechanics of tidal stream energy conversion. Annu. Rev. Fluid Mech. 53, 287–310.

Andritz Hydro Hammerfest, 2021. Renewable energy from tidal currents. Accessed:2021-06-23 https://www.andritz.com/resource/blob/61614/cf15d27bc23fd59db125229506ec87c7/hy-hammerfest--1--data.pdf.

ANSYS, 2018. ANSYS AQWA Theory Manual 19.0. ANSYS, Canonsburg, PA.

Atlantis Resources, 2021. AR1500 tidal turbine. Accessed:2021-06-23 https://simecatlantis.com/wp-content/uploads/2016/08/AR1500-Brochure-Final-1.pdf.

Barltrop, N., Varyani, K.S., Grant, A., Clelland, D., Pham, X.P., 2007. Investigation into wave-current interactions in marine current turbines. Proc. Inst. Mech. Eng. A 221 (2), 233–242.

Blackmore, T., Myers, L.E., Bahaj, A.S., 2016. Effects of turbulence on tidal turbines: Implications to performance, blade loads, and condition monitoring. Int. J. Mar. Energy 14, 1–26.

Brown, S.A., Ransley, E.J., Xie, N., Monk, K., De Angelis, G.M., Nicholls-Lee, R., Guerrini, E., Greaves, D.M., 2021. On the impact of motion-thrust coupling in floating tidal energy applications. Appl. Energy 282, 116246.

Buhl, M.L., 2005. A New Empirical Relationship between Thrust Coefficient and Induction Factor for the Turbulent Windmill State A New Empirical Relationship between Thrust Coefficient and Induction Factor for the Turbulent Windmill State. Technical Report NREL/TP-500-36834.

Cummins, W.E., 1962. The Impulse Response Function and Ship Motion. Report 1661, Department of the Navy, David W. Taylor Model Basin, Hydromechanics Laboratory, Research and Development Report, October 1962.

de Jesus Henriques, T.A., Tedds, S.C., Botsari, A., Najafian, G., Hedges, T.S., Sutcliffe, C.J., Owen, I., Poole, R.J., 2014. The effects of wave–current interaction on the performance of a model horizontal axis tidal turbine. Int. J. Mar. Energy 8, 17–35.

Det Norske Veritas (DNV), 2015. Design of Offshore Steel Structures, General - LRFD Method. Technical Report DNVGL-OS-C101. Standard.

Draycott, S., Payne, G., Steynor, J., Nambiar, A., Sellar, B., Venugopal, V., 2019. An experimental investigation into non-linear wave loading on horizontal axis tidal turbines. J. Fluids Struct. 84, 199–217.

Driscoll, F., Jonkman, J., Robertson, A., Sirnivas, S., Skaare, B., Nielsen, F.G., 2016. Validation of a FAST model of the statoil-hywind demo floating wind turbine. Energy Procedia 94, 3–19.

Ettema, S., 2022. Novel Turbine Fence Optimisation Using Lateral Flow Constraint (Ph.D. thesis). University of Oxford.

Faudot, C., Dahlhaug, O.G., 2012. Prediction of wave loads on tidal turbine blades. Energy Procedia 20, 116–133.

Fernandez-Rodriguez, E., Stallard, T.J., Stansby, P.K., 2014. Experimental study of extreme thrust on a tidal stream rotor due to turbulent flow and with opposing waves. J. Fluids Struct. 51, 354–361.

Galloway, P.W., Myers, L.E., Bahaj, A.S., 2014. Quantifying wave and yaw effects on a scale tidal stream turbine. Renew. Energy 63, 297–307.

Guerra, M., Cienfuegos, R., Thomson, J., Suarez, L., 2017. Tidal energy resource characterization in chacao channel, Chile. Int. J. Mar. Energy 20, 1–16.

Guo, X., Yang, J., Gao, Z., Moan, T., Lu, H., 2018a. The surface wave effects on the performance and the loading of a tidal turbine. Ocean Eng. 156, 120–134.

Guo, X., Yang, J., Lu, W., Li, X., 2018b. Dynamic responses of a floating tidal turbine with 6-DOF prescribed floater motions. Ocean Eng. 165, 426–437.

Hansen, M., 2008. Aerodynamics of Wind Turbines, second ed. International Institute for Environment and Development, London.

Hansen, M.H., Gaunaa, M., Madsen, H.A., 2004. Beddoes-Leishman Type Dynamic Stall Model in State-Space and Indicial Formulations. Technical Report Risoe-R No. 1354(EN), Forskningscenter Risoe.

Hansen, M.O.L., Johansen, J., 2004. Tip studies using CFD and comparison with tip loss models. Wind Energy 7 (4), 343–356. http://dx.doi.org/10.1002/we.126.

Huang, B., Zhao, B., Wang, L., Wang, P., Zhao, H., Guo, P., Yang, S., Wu, D., 2022. The effects of heave motion on the performance of a floating counter-rotating type tidal turbine under wave-current interaction. Energy Convers. Manage. 252, 115093.

ITTC, 2017. Recommended procedures and guidelines: Seakeeping experiments.

Jonkman, J.M., Buhl, M.L.J., 2007. Loads Analysis of a Floating Offshore Wind Turbine Using Fully Coupled Simulation. Technical Report, National Renewable Energy Lab.(NREL), Golden, CO (United States).

Kolekar, N., Vinod, A., Banerjee, A., 2019. On blockage effects for a tidal turbine in free surface proximity. Energies 12 (17), 3325.

Magallanes Renovables, 2021. Technology. Accessed:2021-09-19 https://www.magallanesrenovables.com/technology/.

McNaughton, J., Ettema, S., Zilic de Arcos, F., Vogel, C., Willden, R., 2023. An experimental investigation of the influence of inter-turbine spacing on the loads and performance of a co-planar tidal turbine fence. J. Fluids Struct. 118, 103844.

Milne, I., Day, A., Sharma, R., Flay, R., 2016a. The characterisation of the hydrodynamic loads on tidal turbines due to turbulence. Renew. Sustain. Energy Rev. 56, 851–864.

Milne, I.A., Day, A.H., Sharma, R.N., Flay, R.G.J., 2016b. The characterisation of the hydrodynamic loads on tidal turbines due to turbulence. Renew. Sustain. Energy Rev. 56, 851–864. http://dx.doi.org/10.1016/j.rser.2015.11.095.

Milne, I.A., Sharma, R.N., Flay, R.G., Bickerton, S., 2013. Characteristics of the turbulence in the flow at a tidal stream power site. Phil. Trans. R. Soc. A 371 (1985).

Morison, J.R., Johnson, J.W., Schaaf, S.A., 1950. The force exerted by surface waves on piles. J. Pet. Technol. 2 (05), 149–154.

Ning, S.A., 2014. A simple solution method for the blade element momentum equations with guaranteed convergence. Wind Energy 17 (9), 1327–1345.

Ogilvie, T.F., 1964. Recent progress toward the understanding and prediction of ships motion. In: Proceedings of the 5th Symposium on Naval Hydrodynamics. pp. 3–128.

Orbital Marine Power, 2021. Orbital O2 2MW. Accessed:2021-06-23 https://orbitalmarine.com/O2.

Osman, M.H.B., Willden, R.H.J., 2020. Unsteady loading of a floating tidal turbine oscillating in a pendulum motion. In: Developments in Renewable Energies Offshore. CRC Press, pp. 563–570.

Osman, M.H.B., Willden, R.H.J., Vogel, C.R., 2019. The effects of surge motion on floating horizontal axis tidal turbines. In: Proceedings of the Thirteenth European Wave and Tidal Energy Conference. EWTEC, Naples.

Øye, S., 1991. Dynamic stall simulated as time lag of separation. In: Proceedings of the 4th IEA Symposium on the Aerodynamics of Wind Turbines, Vol. 27. Rome, Italy, p. 28.

Prandtl, L., 1921. Applications of Modern Hydrodynamics to Aeronautics. US Government Printing Office.

Scarlett, G.T., Sellar, B., Van Den Bremer, T., Viola, I.M., 2019. Unsteady hydrodynamics of a full-scale tidal turbine operating in large wave conditions. Renew. Energy 143, 199–213.

Schluntz, J., Willden, R.H.J., 2015. The effect of blockage on tidal turbine rotor design and performance. Renew. Energy 81, 432–441.

Skaare, B., Nielsen, F.G., Hanson, T.D., Yttervik, R., Havmøller, O., Rekdal, A., 2015. Analysis of measurements and simulations from the hywind demo floating wind turbine. Wind Energy 18 (6), 1105–1122.

Tampier, G., Troncoso, C., Zilic de Arcos, F., 2017. Numerical analysis of a diffuser-augmented hydrokinetic turbine. Ocean Eng. 145, 138–147.

Thomson, J., Polagye, B., Durgesh, V., Richmond, M.C., 2012. Measurements of turbulence at two tidal energy sites in puget sound, WA. IEEE J. Ocean. Eng. 37 (3), 363–374.

Wang, S.-q., Li, C.-y., Zhang, Y., Jing, F.-m., Chen, L.-f., 2022. Influence of pitching motion on the hydrodynamic performance of a horizontal axis tidal turbine considering the surface wave. Renew. Energy 189, 1020–1032.

Watanabe, S., Kamra, M.M., Hu, C., 2023. An experimental study of surface wave effects on two interacting tidal turbines. J. Mar. Sci. Technol. 1–12.

Wimshurst, A., Willden, R.H.J., 2016. Tidal power extraction on a streamwise bed slope. Ocean Eng. 125, 70–81. http://dx.doi.org/10.1016/j.oceaneng.2016.08.007.

Zilic de Arcos, F., 2021. Hydrodynamics of Highly-Loaded Axial Flow Tidal Rotors (Ph.D. thesis). University of Oxford.

Zilic de Arcos, F., Vogel, C., Willden, R., 2018. Hydroelastic modelling of composite tidal turbine blades. In: Advances in Renewable Energies Offshore: Proceedings of the 3rd International Conference on Renewable Energies Offshore (RENEW 2018), October 8-10, 2018. Lisbon, Portugal, p. 877.